Comput Geosci (2016) 20:1155–1167
DOI 10.1007/s10596-016-9582-3

# X-ray computed microtomography—a useful tool for petrophysical properties determination

**Jadwiga A. Jarzyna[1] · Paulina I. Krakowska[1] · Edyta Puskarczyk[1] · Kamila Wawrzyniak-Guz[1] · Jakub Bielecki[2] · Konrad Tkocz[2] · Jacek Tarasiuk[3] · Sebastian Wroński[3] · Marek Dohnalik[4]**

Received: 6 May 2015 / Accepted: 21 June 2016 / Published online: 9 July 2016


**Abstract** The main goal of the research was to employ the unique data delivered by various methods to improve the determination of rock reservoir properties. Results of X-ray computed tomography (XRCMT), one of the newest techniques providing high-resolution images of rocks, were used to show that very precise information from this tool is complementary to results from other methods. Standard laboratory measurements (helium pycnometer, mercury injection porosimetry, permeameter) and sophisticated experiments (X-ray computed tomography and nuclear magnetic resonance spectroscopy) were performed to obtain and compare results. Four types of specimens: typical Miocene sandstone-mudstone-claystone rock samples, artificial corundum specimens, shale gas plugs, and limestone sample were investigated to obtain the porosity, permeability, density, and other parameters used in rock descriptions. Mutual relationships between selected groups of rock material properties were presented to provide an integral picture of rock characteristics. The XRCMT results were in general not influenced by lithology, but there were observed shaliness effects on the shape of pores, cross sections, and the tortuosity of porous channels. An analysis of the average porosity and the standard deviation of each XRCMT plot provided information about differences in the heterogeneity of a formation. Thus, the XRCMT method was recommended in pore space parameter determination for microfracture fluid propagation monitoring. There was also observed equivalence between part of the NMR signal from clay-bound water and the XRCMT volume subgroups in porosity/permeability—structural classes I and II. So, the use of the two-subsample approach in the XRCMT interpretation was promoted.

**Keywords** X-ray computed tomography · Nuclear magnetic resonance · Reservoir properties of rocks · Porosity · Permeability

## 1 Introduction

Reservoir properties are crucial rock features for determining the production and injection ability of formations, i.e., the ability for flow-through porous media. The intrinsic properties of individual rock comprise porosity, permeability, shaliness, and water/hydrocarbon saturation. The porosity is further classified as total (including all pores in a rock formation), effective (including the connected pores of diameters allowing flow-through media), and dynamic (using the free fluid index describing the volume of fluid actually produced from a reservoir). Porosity and permeability are closely related based on the mutual relationship between the ability to flow through media and the number of pores and their geometry, the porous cross-sectional area, and the presence of capillaries and fractures. Permeability is mainly based on the connectivity of pores [1]. The mineral

✉ Paulina I. Krakowska
krakow@agh.edu.pl

[1] Department of Geophysics, Faculty of Geology, Geophysics and Environmental Protection, AGH University of Science and Technology, Krakow, Poland

[2] Institute of Nuclear Physics, Polish Academy of Sciences, 31342 Krakow, Poland

[3] Faculty of Physics and Applied Computer Sciences, AGH University of Science and Technology, Krakow, Poland

[4] Oil and Gas Institute – National Research Institute, Krakow, Poland

composition and texture of rock influence the geometry of pores and the size of open throats. It is a well-known rule that greater sorting decreases the porosity and permeability. The tortuosity of porous channels, i.e., the shape of paths through media, highly depends on the geological structure and rock texture.

Permeability is directly measured in the laboratory based on Darcy's law when air, helium, or another gas flows through a core in the steady state. Also used are pressure-decay methods, which are more effective in low-permeability formations [2]. Table 1 (italicized values) shows permeability of the Cambrian tight sandstones with mudstone laminas that have visible microcracks. The measurements were obtained using two techniques: pressure-decay permeability and pulse-decay permeability at the TerraTek Schlumberger Reservoir Laboratory [2]. Citing the TerraTek Glossary,

Pressure-Decay Permeability is a matrix permeability measured on crushed grains of shale or mudstone. Crushed material is orders of magnitude larger than pore structures. Crushing of shales/mudstones allows for the access to pore space and for the removal of artifacts or non-natural features from the rock in order to obtain more accurate data. Pressure decay is only partly valid for silty laminated shales and not valid for sandstones or tight gas sandstones. Pulse-Decay Permeability (mD) is plug permeability, often misinterpreted as an accurate measure of reservoir permeability in shales. Laminated shales are first of all extremely difficult to plug, secondly in plug form, samples contain non-natural artifacts/microfractures from the coring and processing stage of the core analysis which enhance or artificially increase permeability values and sometimes porosity values.

The different values of permeability obtained for the Cambrian tight sandstones illustrate the importance of determining as many parameters as possible to properly characterize a rock formation. Low values of pressure-decay permeability result from an applied methodology and generally present matrix permeability. The difference between the pulse-decay permeability based on the TerraTek results (PDP*) and that based on other laboratory results (PDP**) is a result of the Klinkenberg correction applied to PDP** results [3]. It has also been shown that it is important to make measurements in the same laboratory to get repeatable, credible results.

Various techniques for processing the porosity/permeability results can be found in the literature particularly the fractal approach [4–8]. Researchers in that group focus on the statistical classification and determination of desirable properties of statistically selected groups. Researchers have also preferred a more deterministic approach to the problem of a porous space description to obtain numerical values of the parameters to be used in flow modeling in media [9].

The results of X-ray computed microtomography (XRCMT) are a good source of information on the shape and tortuosity of pore channels, the porous cross-sectional area, and pore connectivity. It is used as the basis for hydrodynamic simulations, and XRCMT is a precise method for obtaining 3D images of investigated rock [10].

Recently, many other applications of X-ray computed microtomography in the geological branches have been presented. Core samples from bioturbated carbonate mudstones constructing a part of the production interval in the Pine Creek gas field of Alberta were imaged using X-ray computed microtomography [11]. Current activity in the recognition of shale gas formation may also benefit from various studies of reservoirs with an unconventional network of micropores. Bioturbation has been recognized in low-permeability, fine-grained rocks [12]. Ichnofossils were identified among others in Lower Marcellus Shale [11]. XRMCT is also a useful tool for identifying gas hydrates and making a detailed recognition of the parameters of gas hydrate deposits. Nadeev et al. [13] used X-ray computed microtomography for the visualization of clay and frozen substances in porous rocks. Other examples combining micro-CT images and micro-XRF results in rock samples reveal the possibility of obtaining common information from the same small part of rock regarding the inner structure of pores and the element composition [14]. Using micro-CT images, it is possible to recognize, image, and evaluate fractures [15, 16]. Madonna et al. [17] presented

**Table 1** Results of permeability measurements using various methods

| Sample name | As-received bulk density [g/cm$^3$] | Pressure-decay permeability [mD] | PDP 500 psi [mD] | PDP 1500 psi [mD] | PDP 3000 psi [mD] | PDP 5000 psi [mD] | PDP* [mD] | PDP** [mD] |
|---|---|---|---|---|---|---|---|---|
| | | | *500* | *1500* | *3000* | *5000* | | |
| C1 | *2.668* | *0.000026* | *0.004302* | *0.000909* | *0.000262* | *0.000087* | *0.0005* | 0.000341 |
| C3 | *2.625* | *0.000032* | *0.006117* | *0.001050* | *0.000336* | *0.000150* | *0.0008* | 0.000560 |

*PDP* pulse-decay permeability, *PDP** pulse-decay permeability interpreted on the basis of TerraTek results,
*PDP*** pulse-decay permeability interpreted on the basis of other laboratory results

the results of elastic wave propagation modeling based on X-ray computed microtomography results. XRMCT can also be used to visualize full core images and to analyze them in terms of the pore space and microfracture orientation in relation to stratification, as well as to identify areas of material sampling for further laboratory measurements [18].

The presented examples show many applications of computed X-ray microtomography and illustrate the necessity of developing the applications of this useful technique in geological and reservoir engineering. Results of other laboratory techniques for determining petrophysical properties are well known and are frequently used in petrophysical practice (for instance [19–23]). The nuclear magnetic resonance spectroscopy (NMR) technique is the most recent one, and others like mercury injection porosimetry, helium pycnometer measurements, and permeameter experiments belong to the special core analyses (SCAL).

In this paragraph, the authors highlighted the known-from-literature applications of X-ray computed microtomography. Also, the importance of and difficulties in reservoir properties determination were pointed out in prospection for standard and unconventional hydrocarbon deposits and table or thermal water reservoirs. The main goal of the research was to employ the unique data delivered by various methods, particularly XRCMT, to improve the determination of rock reservoir properties. The examples included below illustrate the results obtained using available equipment and processing techniques to improve the petrophysical characterization of reservoirs. A unique dataset was employed to demonstrate the capability of XRCMT images in quantifying parameters that may not be captured otherwise and confirm the quality of these results by comparing with outcomes from other techniques.

## 2 Methods and materials

The methods presented in this paper comprise X-ray computed tomography, NMR spectroscopy, mercury injection porosimetry, and standard core laboratory analyses that provide density, bulk density, total porosity, and absolute permeability values.

X-ray computed tomography was performed on core samples in three different laboratories and gave results with different resolutions:

- X-ray microprobe at the Institute of Nuclear Physics, Polish Academy of Sciences, Krakow, Poland (IFJ PAN). This facility consists of a microfocusing X-ray tube (Hamamatsu L9191) with exchangeable targets (Ti, Mo, W, and Ag targets are available), a high-resolution X-ray sensitive CCD camera (Photonics Science VHR-70), and a precise specimen positioning system. The facility allows the imaging of microstructures with a maximum spatial resolution of 4 $\mu$m [24]. During each measurement, 1800 projections were collected, using the high-performance X-ray CCD camera (Photonic Science VHR 70 mm). The camera resolution was 1940 $\times$ 1335 pixels with a 29.4-$\mu$m pixel size. The optical magnification of the system was 30 while the source-camera distance and source-object distance was 60 and 2 cm, respectively. Tomographic reconstructions of samples were carried out using the filtered back projection (FBP) algorithm. Due to the occurrence of the ring artifacts, the ring filter algorithm was used. Rings with a maximum width of 4 pixels and minimum arc length of 90° were removed from the sinograms. In order to determine the empty spaces (pores) and grains of the sample, reconstructions were segmented by thresholding, using the Otsu algorithm. Based on the binarized tomographic reconstruction, the porosity of samples was determinated.
- Nanotom S 180n General Electric Sensing & Inspection Technologies at the Faculty of Physics and Computer Sciences, AGH UST, Krakow, Poland (FPCS AGH UST). This tomograph is equipped with a 57-W X-ray tube with a maximum work voltage of 180 kV. The image is recorded using the Hamamatsu 2300 $\times$ 2300 pixel 2D detector (Ham C 7942CA-02). The maximum spatial resolution in this case is about 500 nm. The reconstruction of measured objects was done with proprietary GE software datosX ver. 2.1.0 with use of Feldkamp algorithm for cone beam X-ray CT. The specimen was scanned at 120 kV of source voltage and 150 $\mu$A X-ray tube current, with a rotation of the specimen of 360° in 2200 steps. The exposure time was 500 ms and a frame averaging of 5 and image skip of 1 were applied. The reconstructed images had a voxel size of 1.5 $\mu$m³. The post reconstruction data treatment was performed using VGStudio Max 2.1. Before the analysis, data was subjected to a filtering process using a 3D median filter with 3D symmetrical kernel 3 $\times$ 3 $\times$ 3 voxels.
- Nikon (X-tek) Benchtop CT 160X microtomograph at the Oil and Gas Institute, Krakow, Poland (OGI). This has X-ray beam-emitting photons with a maximum work voltage of 160 kV. The maximum achievable scanner resolution is approximately 3 $\mu$m [15]. The data segmentation process is based on an image histogram and was performed according to threshold along boundaries method.

Mercury injection porosimetry was realized using the AUTOPORE II 9220 V 2.04 porosimeter at the Department of Fossil Fuels at the Faculty of GGEP, AGH UST, Krakow, Poland. NMR spectroscopy and standard

laboratory measurements were obtained at the Oil and Gas Institute, Krakow, Poland, on a Maran Ultra 7-MHz spectrometer. The permeability and bulk density of artificial specimens were measured in the TerraTek Schlumberger Reservoir Laboratory using the pressure-decay and pulse-decay methods [2].

Results of reservoir properties were obtained for four types of porous, permeable materials. The first group consisted of the typical Miocene sandstone-mudstone-claystone formation with different porosities and permeabilities. The second group was built from an artificial material (corundum specimens), the third one comprised a shale sample, and the fourth was a limestone plug.

## 3 Results and discussion

Comparison of the images from the X-ray computed tomography and also values of porosity and permeability determined using XRCMT with the outcomes from other laboratory methods among four types of data sets are presented in this section. The results of a volume classification of the limestone samples are also presented that broaden the application of XRCMT in rock sample characterization.

### 3.1 Sandstone-mudstone-claystone Miocene formation

Standard laboratory measurements were performed on cores cut from the Miocene sandstone-mudstone-claystone formation in the Polish part of the Carpathian Foredeep (borehole C5k) [25]. XRCMT experiments were conducted for six selected core samples (Table 2) in the IFJ PAN. As results of measurements on the geological samples (volume circa 1 $cm^3$), a series of tomographic cross sections were obtained which were the basis for the porosity calculations and permeability modeling [25, 26]. Simulations of the fluid dynamics in the void spaces of porous media were performed using microtomographic data obtained with high spatial resolution. The lattice Boltzmann method (LBM) in the 3DQ19 geometrical model was used to predict the hydraulic permeability of the media. The multiple-relaxation-time model with halfway-bounce-back boundary conditions was used [26].

Plots of 200 slices for each sample (Fig. 1) illustrate the heterogeneity of the rock formation. The highest variability of porosity was observed in samples M2 and M4: 11.27 and 20.33 %, respectively. The standard deviation, as a measure of porosity variation along the core, was 3.62 and 3.48 %, respectively. It is worth noting that the highest standard deviation is not related to the sample with the highest porosity. Plots of porosity and standard deviation (Fig. 1) revealed differences in the heterogeneity of the formation. The volume of sandstone (VS) and volume of clay (VCL) (results of the comprehensive interpretation of well logs) show the influence of two main lithological components on the porosity. The higher the VS/VCL ratio, the higher the porosity. A small value of the standard deviation was observed in the sample of low VCL (M6). XRCMT results are generally free of lithology, but shaliness, especially in the dispersed type, highly influences the shape of pores and their cross sections as well as the tortuosity of porous channels.

Based on the laboratory results, the relationships between the measured parameters were established to characterize reservoir formation (Fig. 2). Good correlation between porosities from laboratory measurement, i.e., pycnometer ($\Phi$lab) and XRCMT experiment ($\Phi\mu$-CT) (Fig. 2a), may be the basis of a high correlation coefficient between permeabilities in Fig. 2b. Both porosities and permeabilities were determined on the same pieces of rock formation, the same plugs. A similar explanation is related to high correlation between logarithm of permeability (Klab) from standard permeameter measurements and porosity ($\Phi$lab)

**Table 2** Depth-matched results of laboratory measurements and the comprehensive interpretation of well logging in borehole C5k

| Sample | *H* [m] | $\delta$ma [g/cm$^3$] | $\delta$b [g/cm$^3$] | $\Phi$lab [%] | $\Phi\mu$-CT [%] | Klab [mD] | K$\mu$-CT [mD] | $\Phi_{NMR}$ [%] | FFI NMR [%] | $\Phi_{MIP}$ [%] | Ra [$\mu$m] | Ts [m$^2$/g] | VS [%] | VCL [%] |
|---|---|---|---|---|---|---|---|---|---|---|---|---|---|---|
| M1 | 1621.75 | 2696 | 2274 ± 0.027 | 15.66 ± 1.1 | 14.76 ± 2.76 | 20.92 | 24 ± 2 | 18.06 | 10.11 | 8.85 | 0.1799 | 1.967 | 35 | 61 |
| M2 | 1737.9 | 2711 | 2376 ± 0.029 | 12.37 ± 1.14 | 11.27 ± 3.62 | 2.51 | 4 ± 0.5 | 12.82 | 6.73 | 0.03 | 0.1129 | 0.12 | 32 | 64 |
| M3 | 1738.4 | 2719 | 2396 ± 0.029 | 1.15 ± 1.04 | 1.76 ± 0.43 | – | 3 ± 0.5 | 13.09 | 7.03 | 4.55 | 0.1355 | 1.343 | 38 | 56 |
| M4 | 1620.65 | 2735 | 2217 ± 0.027 | 18.93 ± 1.05 | 20.33 ± 3.48 | 168.63 | 170 ± 5 | 19.48 | 16.41 | 8.61 | 0.241 | 1.429 | 56 | 34 |
| M5 | 1625.15 | 2759 | 2.43 ± 0.029 | 11.88 ± 1.15 | 12.41 ± 0.28 | 7.05 | 8 ± 0.5 | 13.1 | 4.9 | 4.23 | 0.0246 | 6.891 | 45 | 50 |
| M6 | 1627.3 | 2751 | 2.27 ± 0.027 | 17.2 ± 1.07 | 20.79 ± 0.37 | 46.5 | 52 ± 2 | 19.26 | 14.77 | 6.01 | 0.0751 | 3.203 | 50 | 40 |

*H* depth; $\delta ma$ specific density; $\delta b$ bulk density; $\Phi lab$ total porosity from standard lab measurements (pycnometer); $\Phi\mu$-*CT* porosity from XRCMT; *Klab* permeability from permeameter measurement; $K\mu$-*CT* permeability modeled from XRCMT and LBM; $\Phi_{NMR}$; *FFI NMR* total porosity and free fluid index from NMR laboratory experiment, respectively; $\Phi_{MIP}$ effective porosity from mercury injection porosimetry; *Ra* radius of pores; *Ts* specific surface; *VS*,*VCL* volume of sandstone and volume of shale, respectively, obtained from the comprehensive interpretation of well logging

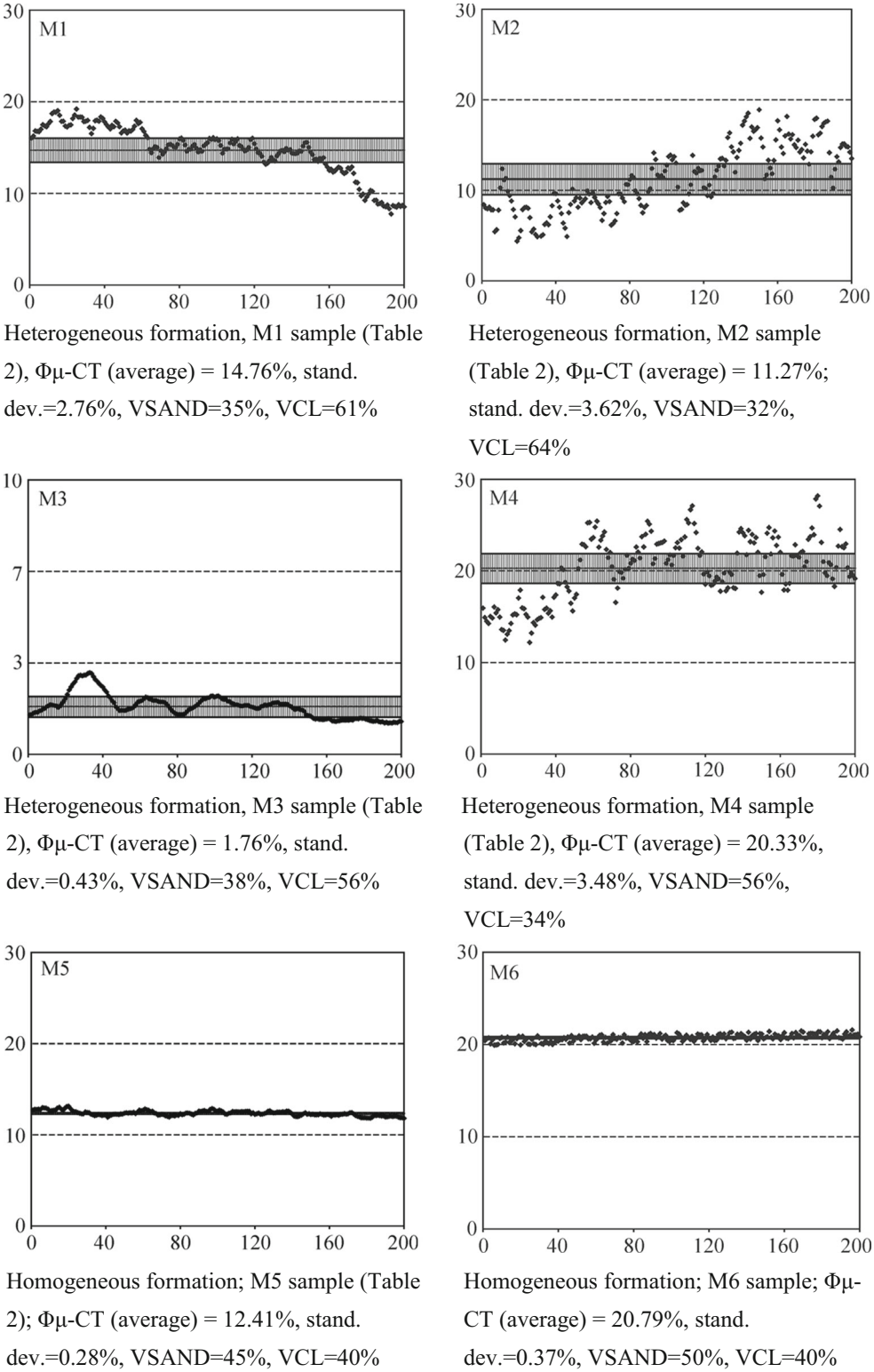


**Fig. 1** Porosity as a result of X-ray computed microtomography measurement and processing, *horizontal axis*—slice number, *vertical axis*—porosity [%]. Slice thickness is equal to 3 $\mu$m

Heterogeneous formation, M1 sample (Table 2), Φμ-CT (average) = 14.76%, stand. dev.=2.76%, VSAND=35%, VCL=61%

Heterogeneous formation, M2 sample (Table 2), Φμ-CT (average) = 11.27%; stand. dev.=3.62%, VSAND=32%, VCL=64%

Heterogeneous formation, M3 sample (Table 2), Φμ-CT (average) = 1.76%, stand. dev.=0.43%, VSAND=38%, VCL=56%

Heterogeneous formation, M4 sample (Table 2), Φμ-CT (average) = 20.33%, stand. dev.=3.48%, VSAND=56%, VCL=34%

Homogeneous formation; M5 sample (Table 2); Φμ-CT (average) = 12.41%, stand. dev.=0.28%, VSAND=45%, VCL=40%

Homogeneous formation; M6 sample; Φμ-CT (average) = 20.79%, stand. dev.=0.37%, VSAND=50%, VCL=40%

(Fig. 2c). The last relationship between logarithm of permeability (K$\mu$-CT) and porosity from XRCMT measurements ($\Phi\mu$-CT) revealed relatively low correlation (Fig. 2d). It means that the assumed LBM model is not fully adequate for these selected plugs. On the basis of a low number of data, it is very difficult to determine proper relationships, especially in inhomogeneous formation, and the presented results show probable relationships.

The results of the NMR experiment, in the form of T2 relaxation time distributions of the Miocene samples,

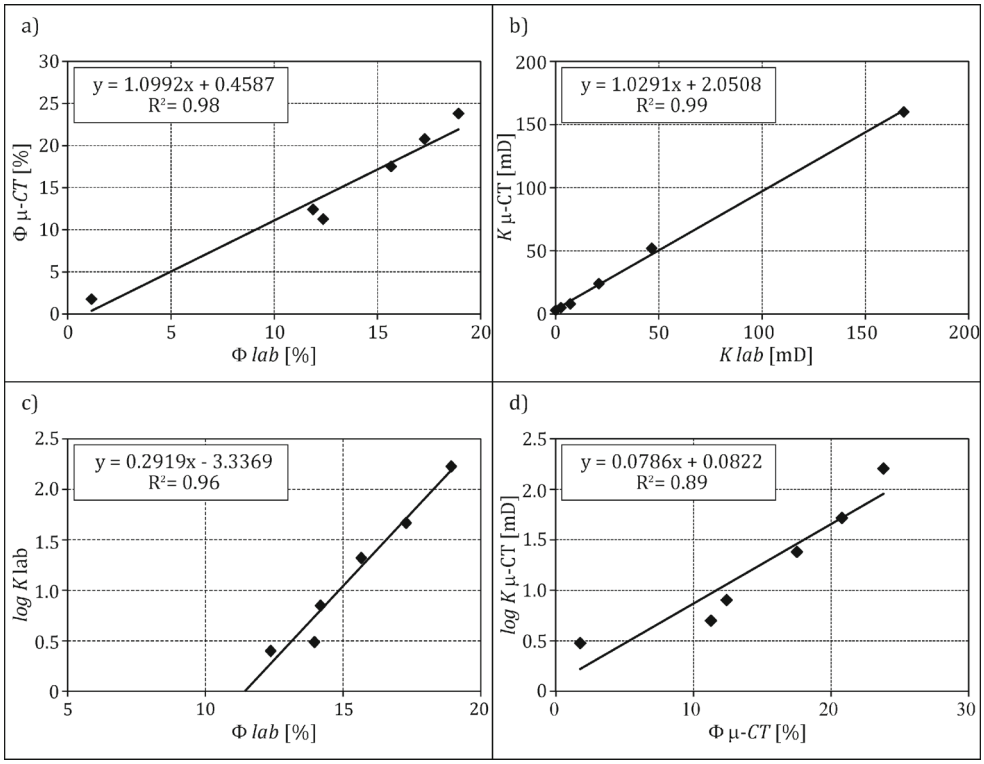


**Fig. 2** Relationships between porosity and permeability from different sources. **a** Porosity obtained from XRCMT experiment ($\Phi\mu$-*CT*) vs. pycnometer porosity ($\Phi$*lab*). **b** Permeability calculated on the basis of XRCMT results ($K\mu$-*CT*) vs. permeameter measurements (*Klab*). **c** Logarithm of permeability (*Klab*) and porosity from standard laboratory measurements ($\Phi$*lab*). **d** Logarithm of permeability ($K\mu$-*CT*) and porosity from XRCMT measurements ($\Phi\mu$-*CT*)

showed similarity in pore space construction (Fig. 3). The T2 distributions are bimodal, which indicates that two pore systems filled with water exist in all samples. The M4 and M6 samples revealed the highest porosity of all the measurement methods (Table 2). Movable water, quantified by the free fluid index (*FFI*), dominates in samples M1, M4, and M6, whereas bound water is predominant in sample M5. FFI is the smallest for this latter sample while the total porosity is quite high [27]. This occurs due to the high shaliness of this sample and the bound water contained in clay minerals. The NMR results complement the outcomes from other methods in that they provide detailed information on porosity and porous space filling. NMR experiments do not give direct information about the pore space shape or tortuosity. The permeability, as a factor responsible for flow in the media pore space, is well correlated with FFI (Fig. 4).

In this group of data, the XRCMT experiment resulted in detailed permeability modeling and good agreement between the measured and modeled values. The NMR measurements are a good supplement to the other results.

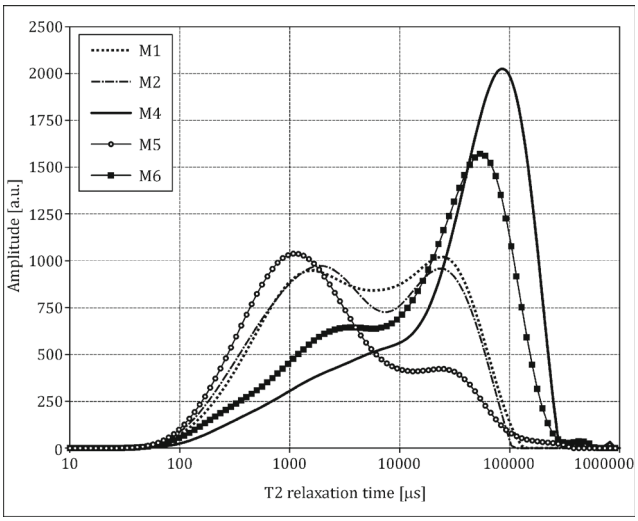


**Fig. 3** T2 distributions for the Miocene samples (Table 2)

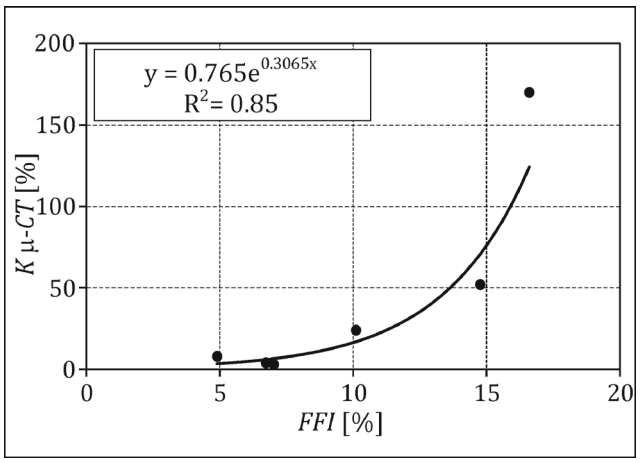


**Fig. 4** Relationship between the permeability modeled based on the porosity from X-ray computed microtomography and the free fluid index (NMR experimental results)

**Table 3** Characteristic parameters of the artificial samples determined from MIP and NMR

| Specimen | Producer info | MIP results | | | | | | NMR results | |
|---|---|---|---|---|---|---|---|---|---|
| | Φ | V1 | S1 | MavV | MavS | Dav | $\Phi_{MIP}$ | $\Phi_{NMR}$ | $\Phi_{NMR\_des}$ |
| | [%] | [mL/g] | [$m^2$] | [$\mu$m] | [$\mu$m] | [$\mu$m] | [%] | [%] | [%] |
| 1530 | 12.1 | 0.032 | 0.971 | 0.209 | 0.065 | 0.131 | 11.95 | 10.63 | 1.74 |
| 1250 | 41.5 | 0.182 | 5.618 | 0.118 | 0.108 | 0.130 | 40.65 | 40.92 | 8.18 |

Φ total porosity determined by producer of artificial samples, *V1* total volume of mercury in pore space, *S1* total specific surface of pores, *MavV* median of pore diameters (from volume), *MavS* median of pore diameters (from surface), *Dav* average pore diameter, $\Phi_{MIP}$ effective porosity calculated on the basis of mercury injection porosimetry, $\Phi_{NMR}$ porosity from nuclear magnetic resonance measured for fully saturated samples, $\Phi_{NMR\_des}$ porosity from nuclear magnetic resonance measured for desaturated samples

The strong correlation between the permeability from the XRCMT (K$\mu$-CT) and the NMR dynamic porosity (FFI) confirmed the ability of accurately determining the permeability while avoiding the difficulties of obtaining direct information about porous space parameters, i.e., pore channel diameters and their tortuosity in the Miocene sandstone-mudstone-claystone formation.

### 3.2 Artificial specimens

X-ray computed microtomography, NMR experiments, and mercury injection porosimetry (MIP) measurements were carried out for two artificial specimens. Corundum samples were produced at the Institute of Ceramics and Building Materials, Warsaw, Poland, to establish porous references that are free of the influence of lithology. These references can be used to compare with known results obtained on well-characterized specimens with rock samples [28]. The characteristic parameters of the artificial samples determined using both methods were compared (Table 3). Very strong correlations between the porosity given by the producer and those obtained from MIP and NMR were observed. A good relationship also exists between the other parameters determined by the mercury injection porosimetry, e.g., the total pore area and porosity.

Mercury injection porosimetry results for both specimens (1530 and 1250) are presented in Fig. 5. The producer of the corundum specimens determined that the porosities of these samples were 12.1 and 41.5 %, respectively, and the MIP values were 11.95 and 40.65 %, respectively. The range of pore diameters was between 0.007 and 176.170 $\mu$m. The results of the NMR experiment for the same specimens are presented in Fig. 5c in the form of T2 distributions. A distinct similarity in the curves is seen in Fig. 5b, c. This is the basis for combining T2 and the radius of the pore space.

Two plots illustrating the relationships between the median of the T2 relaxation time and the quantities from MIP are presented in Fig. 6. These results were obtained for a selected group of Western Carpathian Devonian and Carboniferous rocks of various lithologies (sandstone, claystone, limestone, and dolomite) [29, 30]. Distinct relationships are present between the median of the

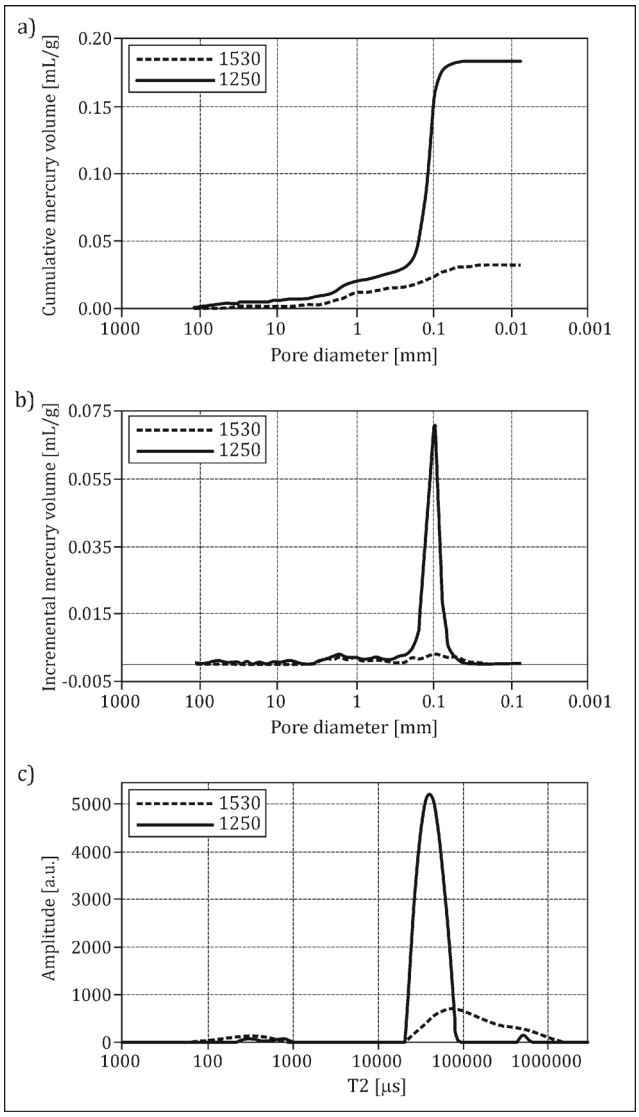


**Fig. 5** MIP and NMR characteristics of the artificial specimens. **a** Cumulative mercury volume in the pore space, **b** incremental mercury volume in the pore space, **c** T2 distributions

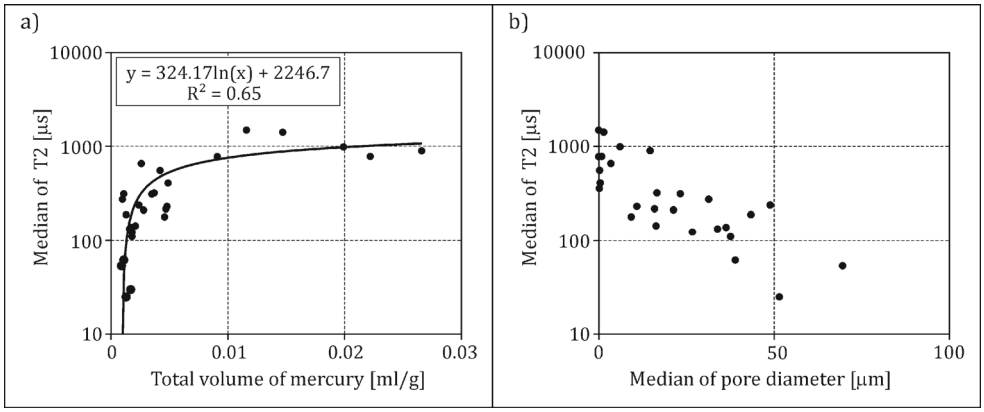


**Fig. 6** Relationships between the median of the T2 relaxation time and the MIP parameters. **a** Median T2 vs. total volume of mercury, **b** median T2 vs. median pore diameter

T2 relaxation time and the total volume of mercury related to effective porosity and close to FFI and the median pore diameter. The results show a real platform for combining the results from both methods.

The MIP porosity results agree with the producer information and NMR values. The agreement between porosity values confirms the credibility of the obtained results. The permeability values from the TerraTek pulse-decay method are the only results available; thus, it was assumed that they are correct (Table 4). In particular, the permeability of specimen 1530 ($\Phi_{MIP} = 11.95$ %) is almost stable. The difference between the results obtained using pressures of 5000 and 500 psi is only 5 %. This means that the fluid flow is steady in that sample. Specimen 1250 ($\Phi_{MIP} = 40.65$ %) revealed a permeability decrease with a pressure increase. The average values of permeability (0.524 and 0.153 mD, respectively) are low in combination with the porosity. Such outcomes are confirmed by the low $\Phi_{NMR\_des}$ results, which means that the majority of pores are not connected.

Specimen 1250 was investigated using the X-ray computed microtomography equipment in the IFJ PAN. A very small volume of the specimen (circa 5 $mm^3$) was used in the measurement. The obtained scans processed in accordance with the porosity determination (Fig. 7) showed a difference in porosity values compared to the results of MIP, NMR, and the producer information. The presented results from two series of porosity calculations (Fig. 7) also revealed a difference. The average porosity calculated on the basis of the left-hand-side microtomographic image (900 slices) equals 24.73 ± 2.80 %, and that on the right-hand side (900 <number of slices <1000) equals 21.51 ± 3.80 %. The presented plots (Fig. 7) showed that the XRCMT method based on a very small part of the rock (Fig. 8) gave inadequate results in the inhomogeneous specimen. Large samples may lead to coarser resolutions of the XRCMT images, which in turn affect the estimates of porosity.

The presented results illustrate that, in the X-ray computed microtomography experiments, the size of the sample is very important, especially in heterogeneous materials. The best measurement resolution was achieved for very small samples (circa 1 mm in diameter). The conclusion is that it is possible to achieve differential parameter values for small pieces of inhomogeneous rocks. One way to get proper and more credible results is to conduct the XRCMT measurement on several plugs taken from the investigated sample.

### 3.3 Shale formation

A Silurian shale sample was investigated using X-ray computed nanotomography. The results provided moderate satisfaction because the geological structure and texture of the sample and its nano-porous space was very difficult to investigate (Fig. 9). The small differences between the specific density (matrix density) and bulk density (density of the sample with porous space) and the extremely low total and effective porosity values confirmed a poorly developed pore structure (Table 5). The white dots in Fig. 9 represent a high-density material, i.e., with high X-ray absorption. The authors' experience suggests probable pyrite mineralization,

**Table 4** Bulk density and pulse-decay permeability results [2]

| Corundum specimen | Bulk density, δb [g/cm³] | Pulse-decay permeability at different pressures [mD] | | | |
|---|---|---|---|---|---|
| | Pressure [psi] | 500 | 1500 | 3000 | 5000 |
| 1250 | 2.319 | 0.548 | 0.529 | 0.514 | 0.503 |
| 1530 | 2.483 | 0.159 | 0.152 | 0.151 | 0.151 |

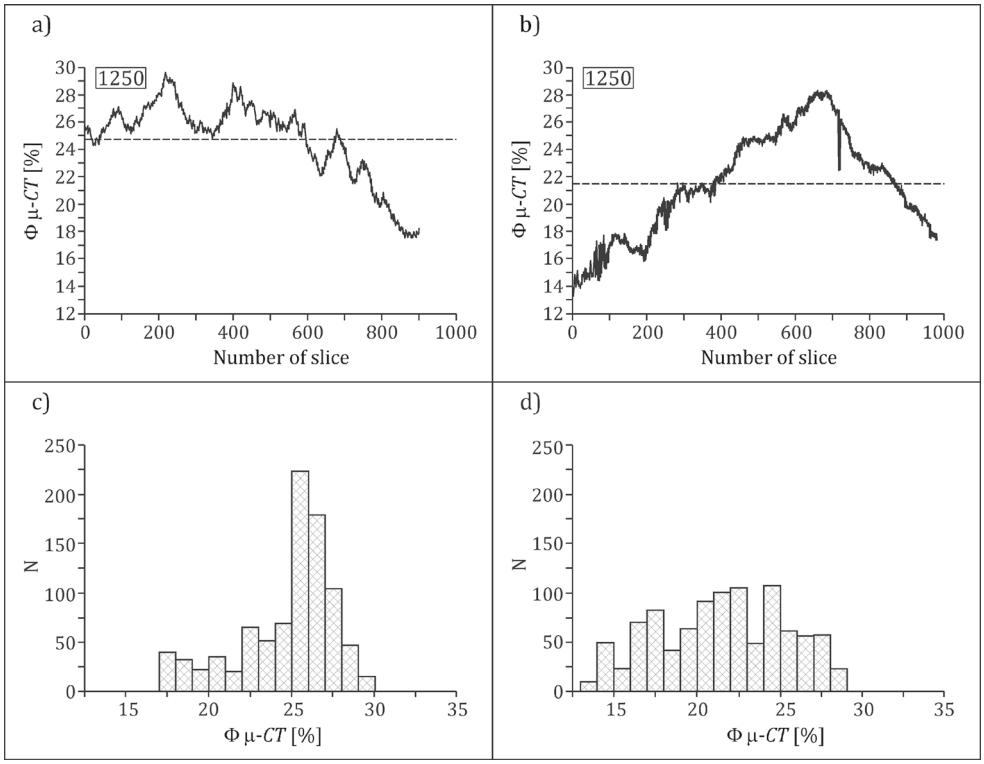


**Fig. 7** Porosity determined for a series of micro-CT slices and frequency histograms related to two reconstructions for sample 1250. Slice thickness is equal to 1 $\mu$m

although XRD analysis did not detect this mineral (Table 5) which may be caused by chance by lack of this mineral in the measured sample. The permeability was measured using the pressure-decay method together with the bulk density at the TerraTek Schlumberger Reservoir Laboratory [2]. The results are $K = 0.044$ nD and $\delta$b= 2.736 g/cm$^3$. Standard petrophysical characteristics of Silurian shale are presented in Table 6. A relatively high bulk density, very close in both measurements (standard—$\delta$b = 2.73 and TerraTek—2.736 g/cm$^3$), allowed the consideration of an admixture of pyrite, although very low porosity is also an indicator of high bulk density.

Pyrite was identified in the Silurian shales from the Lublin sedimentary basin [32] based on the discrepancy in the results from the different methods.

### 3.4 Limestone sample

The Devonian limestone sample (Famennian) was analyzed at the Oil and Gas Institute, Krakow, Poland. Obtained microtomographic images of the limestone sample that reveal pore space heterogeneity are presented in Fig. 10. The process of obtaining a 3D image of the whole sample is time intensive and computationally intensive; therefore,

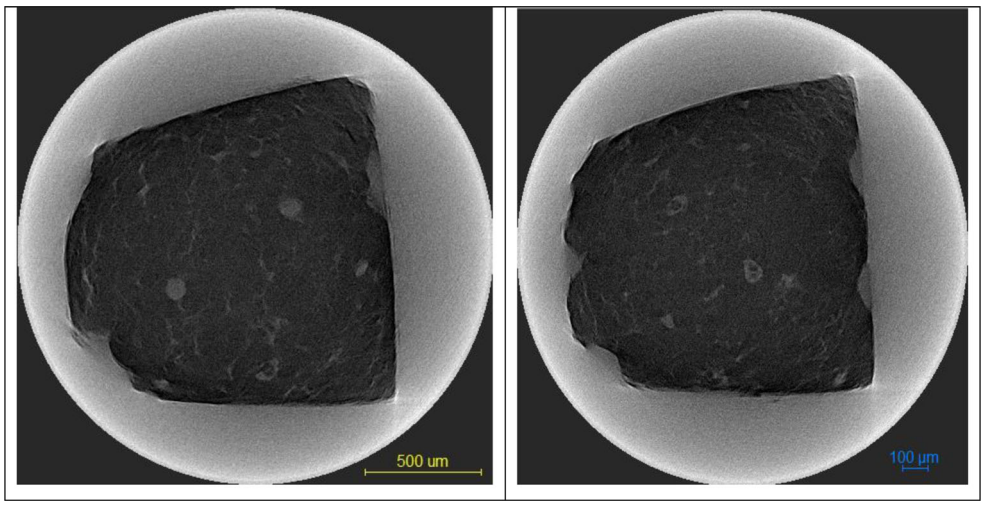


**Fig. 8** Reconstructions of the X-ray computed microtomography image of a small piece of the 1250 corundum specimen

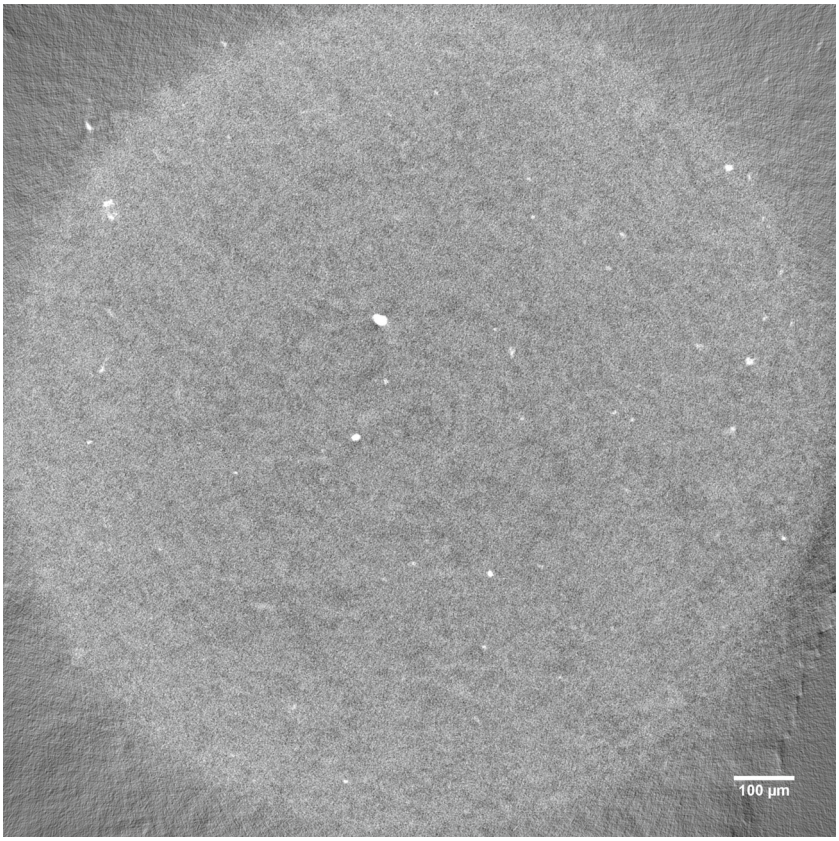


**Fig. 9** Nanotomographic image of the Silurian shale

for the measurements' purposes, the sample is divided into two subsamples, A and B (panels a and c of Fig. 10, respectively). Each subsample represents about a quarter of the total sample volume delivered for analysis. In this way, segmentation occurs with the separation of the pore space of two components: subsamples A and B (Oil and Gas Institute in Krakow approach) [33]. The colors marked in Fig. 10a–d represent subgroups of those pores that are connected with each other but not with the other groups. The limestone sample contains subgroups with volumes in the ranges of 1–9 (class I), 10–99 (class II), 100–999 (class III), 1000–9999 (class IV), 10,000–99,999 (class V), and more than 100,000 voxels (class VI). The volume class shares for two subsamples are presented in Fig. 10b, d. A voxel is the smallest element in a 3D graphic and, in this case, is equal to $5.8 \times 5.8 \times 5.8\ \mu m^3$. A probable microfracture (violet color) is visible in Fig. 10c. XRCMT identification is useful for monitoring microfractures in the fracturing process. An analysis of the petrophysical parameters (Table 7) showed that the pore space of the limestone sample was not well developed. A majority of the NMR signal was detected as Kp1, i.e., from clay-bound water, which was also confirmed by micro-CT measurements. The most numerous subgroups were detected in classes I (yellow) and II (blue) of subgroup volume. Differences in the total porosity from the pycnometer, NMR experiment, and micro-CT measurements resulted from the core sample volume, which was also mentioned in other examples. In cases of pore space complexity, it is recommended that several samples be investigated using the micro-CT technique to improve the obtained information. XRD analysis results showing the mineral composition of the limestone are presented in Table 8.

**Table 5** Results of X-ray diffraction analysis [31]

| Main mineral | Other minerals | Q [%] | Sk [%] | C [%] | D [%] | VCL [%] |
|---|---|---|---|---|---|---|
| Q | Sk, C, D, Ch, M | 33 | 2 | 30 | 2 | 33 |

Q – quartz, Sk – feldspars, C – calcite, D – dolomite, Ch – chlorite, M – micas, VCL – volume of clay minerals

**Table 6** Petrophysical characteristics of Silurian shale [31]

| $H$ | $\delta$ ma | $\delta$ b | $\Phi$ lab | $Kp_1$ | $Kp_2$ | $Kp_3$ | $\Phi_{NMP}$ | $\Phi_{NMP,eff}$ | $\Phi_{MIP}$ | $\Phi\mu$−CT |
|---|---|---|---|---|---|---|---|---|---|---|
| [m] | [g/cm$^3$] | [g/cm$^3$] | [%] | [%] | [%] | [%] | [%] | [%] | [%] | [%] |
| 3246.5 | 2.74 | 2.73 | 1.5 | 0.7 | 0.33 | 0.09 | 1.12 | 0.42 | 0.133 | 0.412 |

$\Phi$lab – total porosity from pycnometer, $Kp_1$ – clay-bound water, $Kp_2$ – capillary-bound water, $Kp_3$ – movable water, $\Phi_{NMR}, eff$ – effective porosity from NMR, $\Phi u - CT$ – total porosity from micro-CT

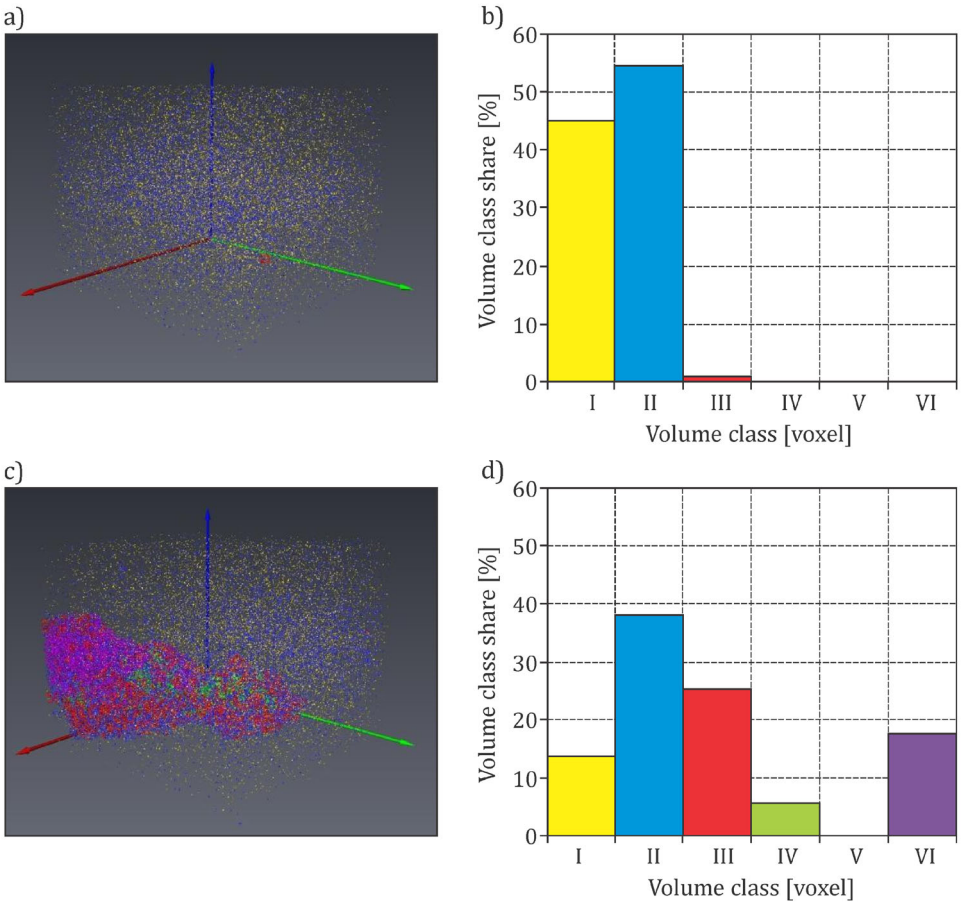


**Fig. 10** X-ray computed microtomography results of the limestone sample. **a** 3D microtomographic image, subsample A, $\Phi lab = 0.4$ %. *Color* of each subgroup's volume: class I—*yellow*, II—*blue*, III—*red*, IV—*green*, V—*white*, and VI—*violet*. **b** Distribution of volume class share, subsample A. **c** 3D microtomographic image, subsample B, $\Phi lab = 1.3$ %. **d** Distribution of volume class share, subsample B

**Table 7** Petrophysical characteristics of limestone sample [31]

| $H$ | $\delta$ma | $\delta$b | $\Phi$lab | $Kp_1$ | $Kp_2$ | $Kp_3$ | $\Phi_{NMP}$ | $\Phi_{NMP,eff}$ | $\Phi_{MIP}$ | $\Phi\mu$-CT |
|---|---|---|---|---|---|---|---|---|---|---|
| [m] | [g/cm$^3$] | [g/cm$^3$] | [%] | [%] | [%] | [%] | [%] | [%] | [%] | [%] |
| 3002.5 | 2.737 | 2.67 | 2.44 | 2.06 | 0.23 | 0 | 2.29 | 0.23 | 0.171 | 0.582 |

Symbols as in Tables 2 and 6

**Table 8** X-ray diffraction analysis results for limestone sample [31]

| Main mineral | Other minerals | C [%] | Q [%] | Sk [%] | D [%] | P [%] | VCL [%] |
|---|---|---|---|---|---|---|---|
| C | Q, Sk, D, Ch, P, M | 54 | 17 | 9 | 8 | 1 | 11 |

*C* calcite, *Q* quartz, *Sk* feldspars, *D* dolomite, *P* pyrite, *Ch* chlorite, *M* micas, *VCL* volume of clay minerals

## 4 Conclusions

X-ray computed microtomography is a powerful technique for rock structure characterization. Combined with NMR experiments and the results of standard laboratory measurements, it can be used to obtain multidimensional information on the rock structure and reservoir properties. Various laboratory measurements based on different physical phenomena improve the credibility of the results. The differences observed in values of the same parameters from various methods were considered as additional petrophysical information.

Hydrocarbon and water prospection in formations of low and very low reservoir parameters requires the use of more and more sophisticated methods to characterize rock properties. X-ray computed tomography is one of the newest techniques that provide high-resolution images of rocks. Heterogeneity of a rock formation is the great obstacle in such investigations. Thus, very precise information from this tool should be confirmed using results from other methods.

The presented data investigated four groups of samples, from the typical Miocene sandstone-mudstone-claystone formation through artificial corundum specimens and shale rock up to a limestone sample. Each material demanded the determination of different features. The investigations of each sample underlined that traps may appear in petrophysical research using the newest techniques. In all the presented examples, X-ray computed tomography revealed parameters and factors that could not be examined using other methods.

The examples included in this paper illustrated the results that could be obtained using available equipment and processing techniques to improve the petrophysical characterization of reservoirs. These examples provided the basis for drawing the following practical conclusions:

- An analysis of the average porosity and the standard deviation of the each XRCMT plot provides information about differences in the heterogeneity of a formation. The higher the sandstone to shale volume ratio, the higher the porosity. Lower values of the standard deviation are characteristic of formations with lower shaliness.
- The XRCMT results are in general not influenced by the lithology. Nevertheless, shaliness affects the shape of pores and the cross sections and tortuosity of porous channels, which are important parameters in the interpretation.
- Pyrite can be identified in the rock sample based on the XRCMT results.
- The XRCMT experiment resulted in detailed data for permeability modeling.
- The XRCMT can be used in the qualitative and quantitative interpretations of pore space parameters and may be used for microfracture propagation monitoring in the hydraulic fracturing process.
- The XRCMT method gave inadequate results in heterogeneous rocks due to the very small rock plug used in the investigation. In rocks with an identified pore space complexity, it is recommended that several plugs be investigated to improve the data.
- The NMR results complemented the outcomes from other methods by providing detailed information on the porosity and saturation of a porous space with clay-bound water, capillary water, and free water.
- There is observed equivalence between part of the NMR signal from clay-bound water (Kp1) and the XRCMT volume subgroups in classes I and II. The use of the two-subsample approach in the XRCMT interpretation is recommended.
- The similarity of the MIP and NMR curves is the basis for combining T2 and the radius of the pore space.
- Artificial samples as references that are free of lithology can be used in the laboratory measurement comparison.
- The obtained relationships between the T2 median and MIP parameters can work as model equations.

**Acknowledgments** This research was financed by statutory funds from the Department of Geophysics, Faculty of Geology, Geophysics and Environment Protection, AGH University of Science and Technology, Krakow, Poland, 2012–2015. Shale and limestone sample research was funded by the National Science Center, Poland, on the basis of decision DEC-2011/03/N/ST10/05354, No. AGH 18.18.140.244. The authors thank Dr. Roman Semyrka, Department of Fossil Fuels at the FGGEP at the AGH UST Krakow, Poland, for performing the mercury injection measurements. The authors' thanks are also directed to prof. dr. hab. Wojciech M. Kwiatek (IFJ PAN) for consultancy and content-related discussions. The authors direct special thanks to the reviewers, whose meaningful remarks made the paper easier to understand.

## References


1. Nolen-Hoeksema, R.: Flow through pores. Oilfield Rev. Autumn. **2014**, 63–64 (2014)
2. TerraTek: Tight rock analysis—permeability. Project nr 20810033, Dec. 22, Report of the TerraTek Schlumberger Reservoir Laboratory. Archive of Department of Geophysics, FGGEP AGH UST, Krakow, Poland (2014)
3. Firouzi, M., Alnoaimi, K., Kovscek, A., Wilcox, J.: Klinkenberg effect on predicting and measuring helium permeability in gas shales. Int. J. of Coal Geol. **123**, 62–68 (2014)
4. Jarzyna, J.A., Bała M.J., Mortimer, Z.M., Puskarczyk, E.: Reservoir parameter classification of a Miocene formation using a fractal approach to well logging, porosimetry and nuclear magnetic resonance. Geophys. Prospect. **61**, 1006–1021 (2013a)
5. Such, P.: Przestrzeń porowa skał łupkowych. Nafta-Gaz **9**, 561–565 (2012)
6. Zinovik, I., Poulikakos, D.: On the permeability of fractal tube bundles. Transp. Porous Media **94**(3), 747–757 (2012)
7. Peveraro, R., Thomas, E.C.: Effective porosity: a defensible definition for shaly sands. SPWLA 51st Annual Logging Symposium, June 19–23 (2010)
8. Leśniak, G., Such, P.: Fractal approach. Analysis of images and diagenesis in pore space evaluation. Nat. Resour. Res. **14**(4), 317–324 (2005)
9. Krakowska, P.I., Madejski, P., Jarzyna, J.: Permeability estimation using CFD modeling in tight Carboniferous sandstone. In: Proceedings of 76th EAGE Conference and Exhibition 2014, 16-19 June, EAGE EarthDoc Database, pp. 1–5 (2014). ISSN 2214-4609, Th P06 05
10. Beard, D.C., Weyl, P.K.: Influence of texture on porosity and permeability of unconsolidated sand. AAPG Bull. **57**(2), 349–369 (1973)
11. Gingras, M.K., Pemberton, S.G., Smith, M.: Bioturbation: reworking sediments for better and worse. Oilfield Review Winter **2015**(/15), 46–60 (2014)
12. Aplin, A.C., Macquaker, J.H.S.: Mudstone diversity: origin and implications for source, seal and reservoir properties of petroleum system. AAPG Bull. **95**(12), 2031–2059 (2011)
13. Nadeev, A., Mikhailov, D., Chuvilin, E., Koroteev, D., Shako, V.: Visualization of clay and frozen substances inside porous rocks using X-ray micro-computed tomography. Micros. Anal. – Tomogr. Suppl. **27**(2), 8–11 (2013)
14. Mutina, A., Bruyndonckx, P.: Combined micro-X-ray tomography and micro-X-ray fluorescence study of reservoir rocks: applicability to core analysis. Microsc. Anal. – Compos. Anal. Suppl. **27**(4), 4–6 (2013)
15. Dohnalik, M.: Improving the ability of determining reservoir rocks parameters using X-ray computed microtomography. Ph.D. Thesis, AGH University of Science and Technology in Krakow. Main Library (2013)
16. Karpyn, Z., Alakmi, A., Parada, C., Grader, A.S., Halleck, P.M., Karacan, O.: Mapping fracture apertures using micro computed tomography. In: International Symposium of the Society of the Core Analysts, 21-24 September, Pau, France, SCA 2003–50 (2003)
17. Madonna, C., Almqvist, B., Seanger, E.: Digital rock physics: numerical prediction of pressure-dependent ultrasonic velocities using micro-CT imaging. Geophys. J. Int. **189**, 1475–1482 (2012)
18. Josh, M., Esteban, L., Delle Piane, C., Sarout, J., Dewhurst, D.N., Clennell, M.B.: Laboratory characterization of shale properties. J. Petrol. Sci. and Eng. **88–89**, 107–124 (2012)
19. Vavra, C.L., Kaldi, J.G., Sneider, R.M.: Geological applications of capillary pressure: a review (1). AAPG Bull. **76**(6), 840–850 (1992)
20. Xiao, L., Mao, Z.Q., Xiao, Z.X., Zhang, C.: A new method to evaluate reservoir pore structure consecutively using NMR and capillary pressure data. SPWLA 49th Annual Logging Symposium 2008, paper AA (2008)
21. Xiao, L., Mao, Z.Q., Wang, Z.N., Yin, Y., Liu, X.G., Xie, B.: Tight gas sands permeability estimation from nuclear magnetic resonance (NMR) logs and mercury injection capillary pressure (MICP) data. Acta Geophys., accepted after reviews (2013)
22. Mohammadlou, M.H., Mork, M.B.: Integrated petrophysical analysis in tight and brecciated carbonate reservoir. Proceedings of the SPE Annual Technical Conference and Exhibition, Florence, Italy, 19-22 September (2010)
23. Jarzyna, J.A., Krakowska, P.I., Puskarczyk, E., Semyrka, R.: Rock reservoir properties from the comprehensive interpretation of nuclear magnetic resonance and mercury injection porosimetry laboratory results. Appl. Magn. Reson. **46**, 95–115 (2015)
24. Bielecki, J., Bożek, S., Lekki, J., Stachura, Z., Kwiatek, W.M.: Applications of the Cracow X-ray microprobe in tomography. Acta Phys. Pol. A **115**(2), 537–541 (2009)
25. Jarzyna, J., Wawrzyniak-Guz, K., Puskarczyk, E., Krakowska, P., Bała, M., Niepsuj, M., Marzec, P., Pietsch, K., Gruszczyk, M. (eds.): Spatial distribution of petrophysical parameters on the basis of laboratory investigations, well logging and seismics, GOLDRUK, Kraków (2013b)
26. Bielecki, J.: Investigations of complex structures by means of the computed microtomography method. Ph.D, Thesis, Library of the Institute of Nuclear Physics Polish Academy of Sciences (2011)
27. Chang, D., Vinegar, H.V., Morris, C., Straley, C.: Effective porosity, producible fluid in carbonates from NMR logging. SPWLA 35th Annual Logging Symposium 1994, paper A (1994)
28. Puskarczyk, E., Jarzyna, J., Kwiatek, W.M., Tkocz, K.: Standard model of rock based on laboratory tests for artificial samples, vol. 198 (2014)
29. Jarzyna, J., Bała, M., Golonka, J., Grabowska, T., Lemberger, M., Pietsch, K., Stefaniuk, M.: New aspects of geophysical measurements interpretation to verify possibility of hydrocarbon prospection in Western Carpathians. Report of the scientific grant MNiI, nr 4T12B 025 28, archive of the Department of Geophysics AGH UST (2005)
30. Jarzyna, J., Puskarczyk, E., Wójcik, A., Semyrka, R.: NMR and mercury porosimetry measurements for the selected rock samples of the Western Carpathians. Geol. 33 **4**(/1), 211–236 (2007)
31. Krakowska, P.: Reservoir potential of the Precambrian and Paleozoic sedimentary rocks on the basis of laboratory measurements and well logging. Ph.D. Thesis, AGH University of Science and Technology in Krakow, Main Library (2014)
32. Porębski, S., Prugar, W., Zacharski, J.: Silurian shales of the East European Platform in Poland—some exploration problems. Geol. Rev. **61**(/11), 630–638 (2013)
33. Kaczmarczyk, J., Dohnalik, M., Cnude, V., Zalewska, J.: The interpretation of X-ray computed microtomography images of rocks as an application of volume image processing and analysis. Proceedings of 18th WSCG International Conference on Computer Graphics, Visualization and Computer Vision, Pilznen, Czech Republic, University of West Bohemia, ISBN 978-80-86943-87-9, 23–30 (2010)